

Article

New Sustainable Approach for the Production of Fe₃O₄/Graphene Oxide-Activated Persulfate System for Dye Removal in Real Wastewater

Md. Nahid Pervez ^{1,2,3} , Wei He ¹, Tiziano Zarra ² , Vincenzo Naddeo ^{2,*}  and Yaping Zhao ^{1,*}

¹ School of Ecological and Environmental Science, Shanghai Key Laboratory for Urban Ecological Process and Eco-Restoration, East China Normal University, Shanghai 200241, China; nahid.tex92@gmail.com (M.N.P.); huanjingjiance@yeah.net (W.H.)

² Sanitary Environmental Engineering Division (SEED), Department of Civil Engineering, University of Salerno, via Giovanni Paolo II 132, 84084 Fisciano (SA), Italy; tzarra@unisa.it

³ Department of Textile Engineering, Southeast University, Tejgaon, Dhaka-1208, Bangladesh

* Correspondence: vnaddeo@unisa.it (V.N.); ypzhao@des.ecnu.edu.cn (Y.Z.);
Tel.: +39-(0)-89-96-9333 (V.N.); +86-(0)-21-54341241 (Y.Z.)

Received: 9 January 2020; Accepted: 5 March 2020; Published: 7 March 2020



Abstract: Persulfate (PS)-activated, iron-based heterogeneous catalysts have attracted significant attention as a potential advanced and sustainable water purification system. Herein, a novel Fe₃O₄ impregnated graphene oxide (Fe₃O₄@GO)-activated persulfate system (Fe₃O₄@GO+K₂S₂O₈) was synthesized by following a sustainable protocol and was tested on real wastewater containing dye pollutants. In the presence of the PS-activated system, the degradation efficiency of Rhodamine B (RhB) was significantly increased to a level of ≈95% compared with that of Fe₃O₄ (≈25%). The influences of different operational parameters, including solution pH, persulfate dosage, and RhB concentration, were systemically evaluated. This system maintained its catalytic activity and durability with a negligible amount of iron leached during successive recirculation experiments. The degradation intermediates were further identified through reactive oxygen species (ROS) studies, where surface-bound SO₄^{•−} was found to be dominant radical for RhB degradation. Moreover, the degradation mechanism of RhB in the Fe₃O₄@GO+K₂S₂O₈ system was discussed. Finally, the results indicate that the persulfate-activated Fe₃O₄@GO catalyst provided an effective pathway for the degradation of dye pollutants in real wastewater treatment.

Keywords: persulfate activation; dyes; wastewater treatment; Fe₃O₄; graphene

1. Introduction

Water pollution is regarded as one of the most important issues worldwide due to its harmful and dangerous impact on ecosystems and human health. Dye effluent, especially, has become a major source of water pollution and is very difficult to degrade due to its high toxicity and carcinogenicity [1,2]. Therefore, it is highly desirable to build constructive and useful technologies for degrading the dye pollutants from wastewater.

In past decades, significant efforts have been made regarding Fenton-based advanced oxidation processes (AOPs) as the effective techniques for the wastewater treatment, where iron(II) sulfate (Fe²⁺) is used as the catalyst and hydrogen peroxide (H₂O₂) is treated as the oxidant [3]. This oxidation process occurs mainly via the production of hydroxyl radicals (•OH). Nevertheless, the lower oxidation potential, a strict pH range (2–4), a higher amount of iron-containing sludge, and stability remain challenges [4]. Recently, persulfate (PS)-based AOPs have exhibited great promise toward degrading pollutants by overcoming these limitations [5]. PS can generate sulfate radicals (SO₄^{•−}), which possess

many advantages, such as a higher redox potential, wide pH range (2–11), longer life span, and more efficiency over $\bullet\text{OH}$ that enables excellent electron transfer of the oxidant toward higher contaminant degradation [6,7]. In general, the production of sulfate radicals can be obtained through PS activation by using several strategies, such as heat, ultraviolet, ultrasound, transition metal ions, carbonaceous-based materials, base, phenol, glucose, and ascorbic acid [8]. Consequently, transition-metal-based catalysts have been widely utilized as a PS activator due to their excellent catalytic efficiency [9]. However, the drawbacks of transition-metal-based catalysts for inhomogeneous systems include poor removal efficiency, precipitation of iron (III) as sludge, and less reusability, which has hindered their widespread use [10]. Hence, transition-metal-based heterogeneous catalyst systems have received tremendous attention for PS activation because of their environmentally friendly nature, high performance, simple operation stability, and high availability [11].

Iron (Fe)-based heterogeneous catalyst materials (e.g., Fe_3O_4) have received much attention regarding frequently activating PS because of their high natural abundance, low price, and they could easily prevent secondary pollution through their recovery performance [12]. However, Fe_3O_4 nanoparticles usually tend to aggregate in the solution, which can decrease their surface area and cause lower stability and catalytic efficiency [13]. Taking this into consideration, it is necessary to use a proper support that can enhance their overall performance. Graphene has been widely reported to be an emerging supporting material for metal oxides due to its high surface area, chemical stability, mechanical stability, and electronic properties [14]. Several studies have focused on graphene as a supporting carrier of metal-oxide-based nanoparticles for preventing their agglomerative nature [15,16]. Therefore, the application of graphene oxide into Fe_3O_4 particles can be used to prevent Fe_3O_4 agglomeration and enhance the PS-based AOP's performance through the synergistic effect between the catalysis and adsorption. Additionally, the magnetization property of Fe_3O_4 may promote the separation efficiency of the catalyst from the solution. The application of Fe_3O_4 /graphene nanocomposite has been widely investigated regarding activating H_2O_2 for organic pollutants degradation [17,18], while PS activation by Fe_3O_4 /GO nanocomposites for pollutants removal from wastewater is seldom reported. For example, Gong et al. [19] prepared a solvothermal-based Fe_3O_4 /GO nanocomposite with a persulfate activated system for the removal of methylene blue, but this method requires a higher temperature and more time, which limits its feasibility for further uses.

Therefore, in the present work, a novel Fe_3O_4 @GO nanocomposite was successfully prepared using a precipitation method with non-toxic materials requiring a low temperature and time as a sustainable protocol, which has not been reported before to the author's best knowledge. The composite was verified using different characterization techniques, such as field emission scanning electron microscopy (FE-SEM), transmission electron microscopy (TEM), and X-ray diffraction patterns (XRD). Then, the catalytic performance of the Fe_3O_4 @GO catalyst in persulfate activation for Rhodamine B (RhB) degradation was examined in detail. The most common industrial dye, RhB, was selected because of its harmful effects on the environment [20]. The influence of the operational conditions, such as the initial solution pH, PS dosages, and RhB concentration were thoroughly studied. The effect of the iron species, salt, and coexisting dyes (Methylene blue (MB) and Orange II (OII)) on RhB degradation was also investigated. A possible RhB degradation pathway was proposed, and a radical mechanism in the Fe_3O_4 @GO+ $\text{K}_2\text{S}_2\text{O}_8$ system was speculated using quenching experiments. Additionally, the treatment efficiency of real wastewater containing RhB, MB, and OII dyes was checked in the presence of the Fe_3O_4 @GO+ $\text{K}_2\text{S}_2\text{O}_8$ system.

2. Experimental Materials and Methods

2.1. Reagents and Materials

Natural flakes of graphite were kindly supplied by Guangfu Fine Chemicals Company Limited (Tianjin, China) and used as received. Ascorbic acid, potassium persulfate, DMPO (5,5-dimethyl-1-pyrroline N-oxide, 98 %), coumarin, and TEMP (2,2,6,6-tetramethyl-4-piperidinol, 97%)

were received from Sigma-Aldrich Trading Co., Ltd (Shanghai, China). Tetranitromethane (TNM), tert-butyl alcohol (TBA), ferrous sulphate ($\text{FeSO}_4 \cdot 7\text{H}_2\text{O}$), and potassium iodide (KI) was bought from Aladdin Chemical Ltd. (Shanghai, China). Rhodamine B (RhB), methanol (MeOH), orange II (OII), ammonium hydroxide (25% *v/v*, $\text{NH}_3 \cdot \text{H}_2\text{O}$), and methylene blue (MB) were bought from Sinopharm Chemical Reagent Ltd. (Shanghai, China). All of the other materials and chemicals used in this work were of analytical purity, and deionized water was used for making the experimental solutions.

2.2. Synthesis of $\text{Fe}_3\text{O}_4@\text{GO}$

The catalyst $\text{Fe}_3\text{O}_4@\text{GO}$ was created by following a precipitation method. Initially, the preparation of graphene oxide (GO) was synthesized based on the Hummers method [21]. Then, the synthesis of the catalyst was started by adding a known amount of GO (0.1 g) and $\text{FeSO}_4 \cdot 7\text{H}_2\text{O}$ (2.78 g) into 100 mL of DI water and ultrasonically treated the mixture for 30 min to receive a unique dispersion of $\text{Fe}_3\text{O}_4@\text{GO}$. The final pH = 11.0 of the solution was achieved by adjusting with 25% ammonium hydroxide. Then, the solution was magnetically stirred in a water bath at 95 °C for 4 h to obtain a $\text{Fe}_3\text{O}_4@\text{GO}$ nanocomposite. The obtained $\text{Fe}_3\text{O}_4@\text{GO}$ nanocomposite was washed two times with DW and dried using the lyophilization method for further subsequent experiments. The bare Fe_3O_4 was prepared by following the same experimental procedure in the absence of GO dispersion.

2.3. Characterization

Transmission electron microscopy (TEM) (JEOL-2100, Hitachi, Tokyo, Japan) and a field emission scanning electron microscopy (FE-SEM, Hitachi S-4800, Tokyo, Japan) were employed to investigate the surface morphological properties of the prepared catalyst. The crystallographic characteristics of the prepared catalysts were investigated using an X-ray diffractometer (Rigaku D/Max-2500, Tokyo, Japan) at room temperature using a $\text{CuK}\alpha$ radiation source. The detection of the elemental composition of the catalyst was revealed through an Axis ultra-X-ray photoelectron spectroscopy (XPS) (Kratos Instrument, Kyoto, Japan). The functional groups were identified with a Nicolet 8700 Fourier-transform infrared spectrometer (Perkin Elmer, Shelton, CT, USA) using a KBr pellet system in the range of 4000–550 cm^{-1} . A Hitachi U-4100 spectrophotometer was used to analyze the UV-vis diffuse reflectance spectra (DRS) of the catalyst with barium sulphate as the reference sample. A fluorescence spectrophotometer (Hitachi F-4500, Tokyo, Japan) was used to test the photoluminescence (PL) properties of the catalyst.

2.4. Catalytic Tests of Persulfate-Activated $\text{Fe}_3\text{O}_4@\text{GO}$

The batch catalytic degradation procedures of RhB were evaluated in a cylindrical borosilicate glass reactor (dimension: 15 cm \times 7 cm). In a typical test, a certain amount of $\text{Fe}_3\text{O}_4@\text{GO}$ (200 mg) and $\text{K}_2\text{S}_2\text{O}_8$ (1.5 mM) were subsequently dissolved into a 400 mL RhB (20 mg L^{-1}) solution to initiate the reaction. The mixed solution was magnetically stirred at 20 °C in a natural pH medium throughout the reaction process. After that, samples (5 mL) of the solution were withdrawn at preset time intervals and separated using a magnet. Then, UV-vis spectra were used to monitor the degradation behavior of RhB using a UV-vis spectrophotometer (UV-3900, Shimadzu, Tokyo, Japan) at the maximum absorption wavelength of RhB (554 nm). The RhB decolorization efficiency (%) was calculated using the following Equation (1):

$$\text{Decolorization (\%)} = \frac{C_0 - C_t}{C_0} \times 100 \quad (1)$$

where C_0 represents the initial concentration of RhB and C_t denotes the concentration of RhB at a determined time interval. The durability of $\text{Fe}_3\text{O}_4@\text{GO}$ was measured by conducting six consecutive adsorption–oxidation cycles experiments. After every cycle, the used catalyst was washed 2–3 times with DI water to remove residual dyes and was separated using a magnet before starting the next cycle.

2.5. Analytic Methods

The measurement of the persulfate decomposition was investigated according to the reference [22]. The total leakage amount of Fe was investigated using an inductively coupled plasma-mass spectrometry (ICP-MS, OPTIMA8000, PE, USA instrument). The mineralization performance was recorded using a Shimadzu 5050 (Tokyo, Japan) total organic carbon (TOC) analyzer. To identify the main oxidizing species in the $\text{Fe}_3\text{O}_4\text{@GO}+\text{K}_2\text{S}_2\text{O}_8$ system, a series of scavengers, namely NaN_3 (sodium azide), TBA (tert-butyl alcohol), KI (potassium iodide), AA (ascorbic acid), and MeOH (methanol), were added in the catalytic experiments [23]. A Hitachi F-4500 fluorescence spectrometer was employed to identify $\bullet\text{OH}$ and $\text{O}_2^{\bullet-}$ radicals at a wavelength of 332 nm using coumarin [24] and the tetranitromethane was used to generate the $\text{O}_2^{\bullet-}$ with a UV-vis spectrophotometer [25]. The generated reactive radicals were further detected using an electron paramagnetic resonance (EPR) spectrometer (JES-FA200, Bruker, Bremen, Germany).

3. Results and Discussion

3.1. Properties of $\text{Fe}_3\text{O}_4\text{@GO}$

The XRD patterns of the synthesized $\text{Fe}_3\text{O}_4\text{@GO}$ nanocomposite, Fe_3O_4 , and GO with typical characteristics are shown in Figure 1a. For GO, there was only a broad peak at $2\theta = 10.6^\circ$ assigned to the (002) plane, which appeared due to the existence of abundant oxygen-containing functional groups in the GO structure. The typical XRD pattern for Fe_3O_4 exhibited peaks at 2θ of 18.3° , 30.2° , 35.8° , 43.6° , 53.6° , 57.3° , and 64.1° , which corresponded to the indices (111), (220), (311), (400), (422), (511), and (440), respectively. The XRD diffraction peaks of the $\text{Fe}_3\text{O}_4\text{@GO}$ nanocomposite were indexed to the standard data of pure Fe_3O_4 (JCPDS card, file no. 19-0629) [26]. These peaks displayed a strong and narrow shape, indicative of a higher crystalline nature. However, it was noticed that the diffraction peak of GO was absent in the $\text{Fe}_3\text{O}_4\text{@GO}$; the reason may be that the crystalline structures of GO were changed through the intercalation of Fe_3O_4 nanoparticles in the GO layers during synthesis.

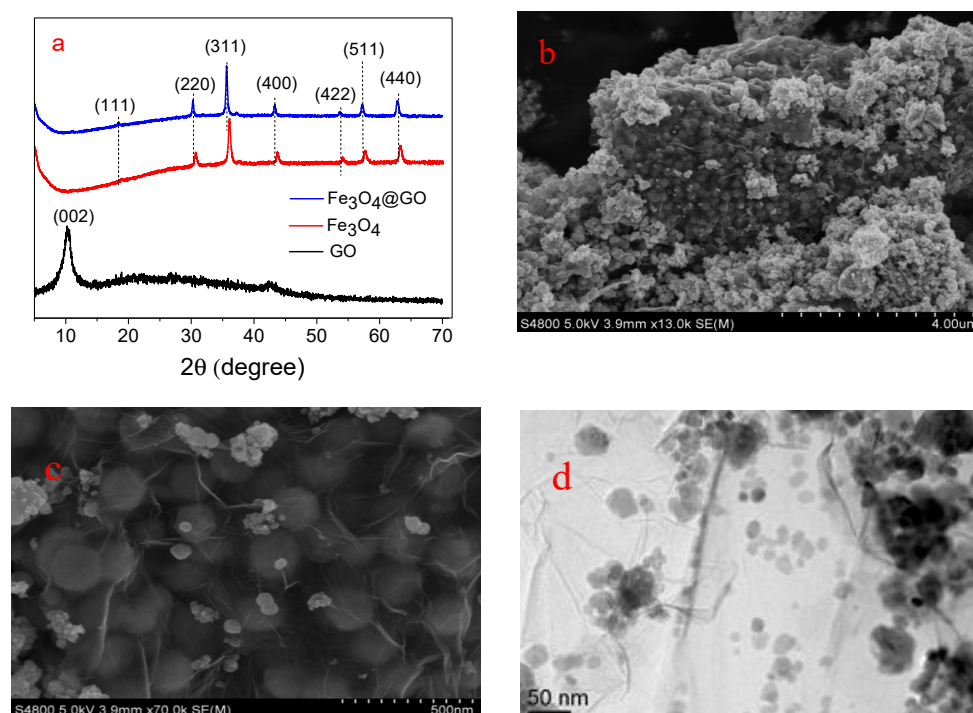


Figure 1. (a) XRD spectra for GO, Fe_3O_4 , and $\text{Fe}_3\text{O}_4\text{@GO}$; (b) SEM images of $\text{Fe}_3\text{O}_4\text{@GO}$; and (c,d) TEM images of Fe_3O_4 and $\text{Fe}_3\text{O}_4\text{@GO}$, respectively.

The surface morphology and structure of the Fe_3O_4 and $\text{Fe}_3\text{O}_4@\text{GO}$ nanocomposite were identified using SEM and TEM images. Regarding the morphology of Fe_3O_4 , the SEM image showed a fiber-like structure with very small particles (Figure 1b) and the TEM image of Fe_3O_4 (Figure 1c), which determined the shape of the majority of particles, were spherical and formed agglomerated structures, which could be due to the magnetism properties of Fe_3O_4 . Additionally, the morphology of the $\text{Fe}_3\text{O}_4@\text{GO}$ nanocomposite demonstrated that the entire spherical surface of the GO sheets was covered by a certain amount of irregular small Fe_3O_4 particles at a higher density (Figure 1d).

3.2. Synergistic Activation of Persulfate Using $\text{Fe}_3\text{O}_4@\text{GO}$

The degradation percentages of RhB in different systems were evaluated and the results are shown in Figure 2. As can be seen, the use of Fe_3O_4 resulted in 10% RhB degradation after a 120-min reaction time. Then, partial improvement of the RhB removal efficiency (<25%) was noticed by using $\text{Fe}_3\text{O}_4@\text{GO}$, which was attributed to the higher surface area of GO accelerating the mass transfer of the substrates. To verify the influence of persulfate on the RhB degradation, experiments were conducted with the persulfate system. Initially, it was found that a slightly higher RhB degradation efficiency (<30%) was achieved with $\text{K}_2\text{S}_2\text{O}_8$ alone; meanwhile, 35% RhB could be degraded through the incorporation of Fe_3O_4 into the $\text{K}_2\text{S}_2\text{O}_8$ solution. This suggests that the $\text{Fe}_3\text{O}_4 + \text{K}_2\text{S}_2\text{O}_8$ system had a higher impact on the RhB degradation efficiency due to the activation of $\text{K}_2\text{S}_2\text{O}_8$ by Fe_3O_4 nanoparticles. However, the RhB degradation efficiency was improved significantly in the presence of the $\text{Fe}_3\text{O}_4@\text{GO} + \text{K}_2\text{S}_2\text{O}_8$ system, with more than 95% RhB degraded within 120 min. These results demonstrate that the $\text{Fe}_3\text{O}_4@\text{GO}$ system could strongly activate $\text{K}_2\text{S}_2\text{O}_8$ to produce sulfate radicals ($\text{SO}_4^{\bullet-}$), which facilitated the effective RhB degradation. Compared to pure Fe_3O_4 , the catalytic activity of the $\text{Fe}_3\text{O}_4@\text{GO}$ system was highly efficient for $\text{K}_2\text{S}_2\text{O}_8$ activation to degrade RhB due to the synergistic effect between GO and Fe_3O_4 . The RhB degradation behavior followed the pseudo-first-order kinetics model and was fitted with Equation (2) [27]:

$$\ln\left(\frac{C_t}{C_0}\right) = -kt \quad (2)$$

where C_0 represents the initial RhB concentration, C_t is the concentration of RhB at a given time, and k is the value of the kinetic rate constant. Table 1 represents the results of the pseudo-first-order kinetics with their corresponding R^2 values. It was noticed that the presence of the $\text{Fe}_3\text{O}_4@\text{GO} + \text{K}_2\text{S}_2\text{O}_8$ system revealed the highest reaction rate constant among all of the used catalysts. These results indicate that a significant synergistic effect was exhibited in the $\text{Fe}_3\text{O}_4@\text{GO} + \text{K}_2\text{S}_2\text{O}_8$ combined system, which was revealed as being the most efficient for RhB degradation.

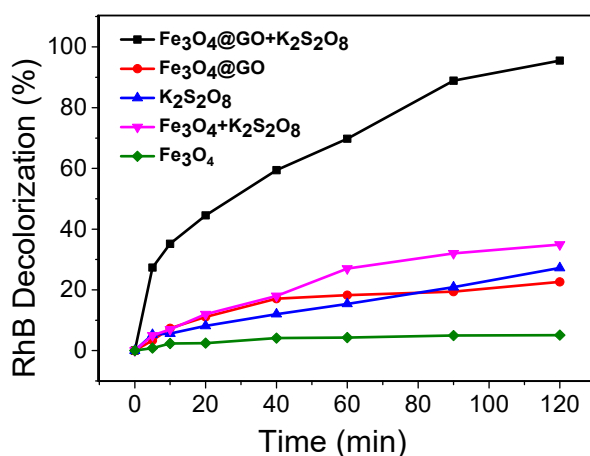


Figure 2. Decolorization of Rhodamine B (RhB) under different conditions with time. Reaction conditions: 200 mg catalyst + 20 ppm RhB + 1.5 mM $\text{K}_2\text{S}_2\text{O}_8$ + 4.34 pH + agitate at room temperature (20 °C).

Table 1. Kinetic rate constants of the pseudo-first-order model.

Reaction Type	Rate Constant (min ⁻¹)	R ²
Fe ₃ O ₄	0.0004	0.7884
K ₂ S ₂ O ₈	0.0024	0.9843
Fe ₃ O ₄ @GO	0.0020	0.8426
Fe ₃ O ₄ + K ₂ S ₂ O ₈	0.0036	0.9575
Fe ₃ O ₄ @GO + K ₂ S ₂ O ₈	0.0239	0.9774

3.3. Influence of the Operational Parameters

3.3.1. Effect of pH

The initial solution pH is regarded as a significant factor that may impact on the performance of the heterogeneous persulfate activation process. Therefore, the RhB degradation efficiency was investigated by varying the solution pH range from 3.02 to 10.02 (Figure 3a). As presented, the RhB degradation percentages were reduced greatly for a 120 min reaction period with the higher values of the solution pH. The highest degradation percentage of RhB (95.3%) was obtained at pH 4.34. The possible reasons for this may be that sulfate radicals are more stable in acidic conditions and could also impact the surface properties of the catalyst. Previous works also proved that the degradation performance of pollutants was better under acidic conditions [28]. However, the RhB degradation efficiency was inhibited by the increased solution pH because of precipitation and the slower oxidation of dissolved Fe²⁺. It was reported that the scavenging of SO₄^{•-} by •OH occurred at higher pH values, resulting in a lower degradation efficiency [29]. Additionally, the lifetimes of SO₄^{•-} and •OH radicals were reduced at higher pH ranges because they were unable to diffuse into the bulk phase properly to degrade the pollutants. Xu et al. [30] found similar lower degradation efficiencies for trichlorophenol at higher pH values. These results indicate that acidic and neutral pH values were much more beneficial than alkaline pH for RhB degradation efficiency in this study. The pH evolution changes were investigated under different initial pHs during the degradation studies of RhB (Figure 3b). As can be seen, the final pH changed rapidly when the initial pH was below ≈9 due to the major radical (SO₄^{•-}) being strongly active in acidic conditions; however, the final pH did not change significantly in the initial pH range of 9–10 because of the formation of strong buffer intermediates. The evolution of PS at different initial pH values was investigated (Figure S1). It was noticed that the decomposition of PS was higher at acidic and neutral pHs, i.e., 4.34 and 6.02, but slower PS decomposition was observed at an alkaline pH (10.02), indicating that PS is more effective in acidic and neutral conditions at producing a higher number of active radicals and accelerating the efficiency of RhB degradation relative to alkaline conditions. Furthermore, the RhB degradation efficiency under various initial pHs and the decomposition rate of PS coincided, demonstrating that PS was consumed exclusively rather than via self-decomposition. Overall, these results revealed that acidic and neutral conditions were beneficial for RhB degradation in the Fe₃O₄@GO + K₂S₂O₈ system, which is more useful for practical applications.

3.3.2. Effect of Persulfate Dosage

The proper amount of persulfate dosage must be identified, as it is the source of the reactive oxygen species (ROS) that are accountable for the RhB oxidation. Meanwhile, it is important to prevent an excess amount of PS use in the catalytic system in terms of both economic feasibility and the scavenging effect of PS on the production of SO₄⁻ radicals. Therefore, the effect of PS dosage on RhB degradation efficiencies in the Fe₃O₄@GO + K₂S₂O₈ system was investigated while keeping other operating parameters constant. As shown in Figure 3c, the degradation efficiency of RhB was only 35.4% after 120 min in the absence of PS. In contrast, a gradual increase in the RhB degradation efficiency was observed upon increasing the dosage of PS. However, increasing the dosage of PS up to 1.5 mM revealed a significant amount of RhB degradation whereby 93.4% could be obtained. This

phenomenon occurred because a higher concentration of PS was favorable for the production of more reactive radicals and it interacted with the surface of the catalyst and easily reacted with Fe^{2+} , which facilitated improved RhB degradation. The degradation efficiency of RhB decreased slightly when the PS dosage further increased up to 2–2.5 mM, which could be ascribed to insufficiently activated radicals supported by the higher rate of reaction between the radicals and the PS [31]. It is of note that an increment in the dosage of PS did not induce a higher degradation efficiency was obtained when the dosage of persulfate was beyond a certain value because excess PS acted as a scavenger of $\text{SO}_4^{\bullet-}$ radicals and formed $\text{SO}_4^{\bullet-}$. Therefore, the decrease of RhB degradation efficiency toward accommodating a saturation condition at a higher PS dosage can be assigned to the inhibiting effect of superfluous $\text{S}_2\text{O}_8^{2-}$ [32].

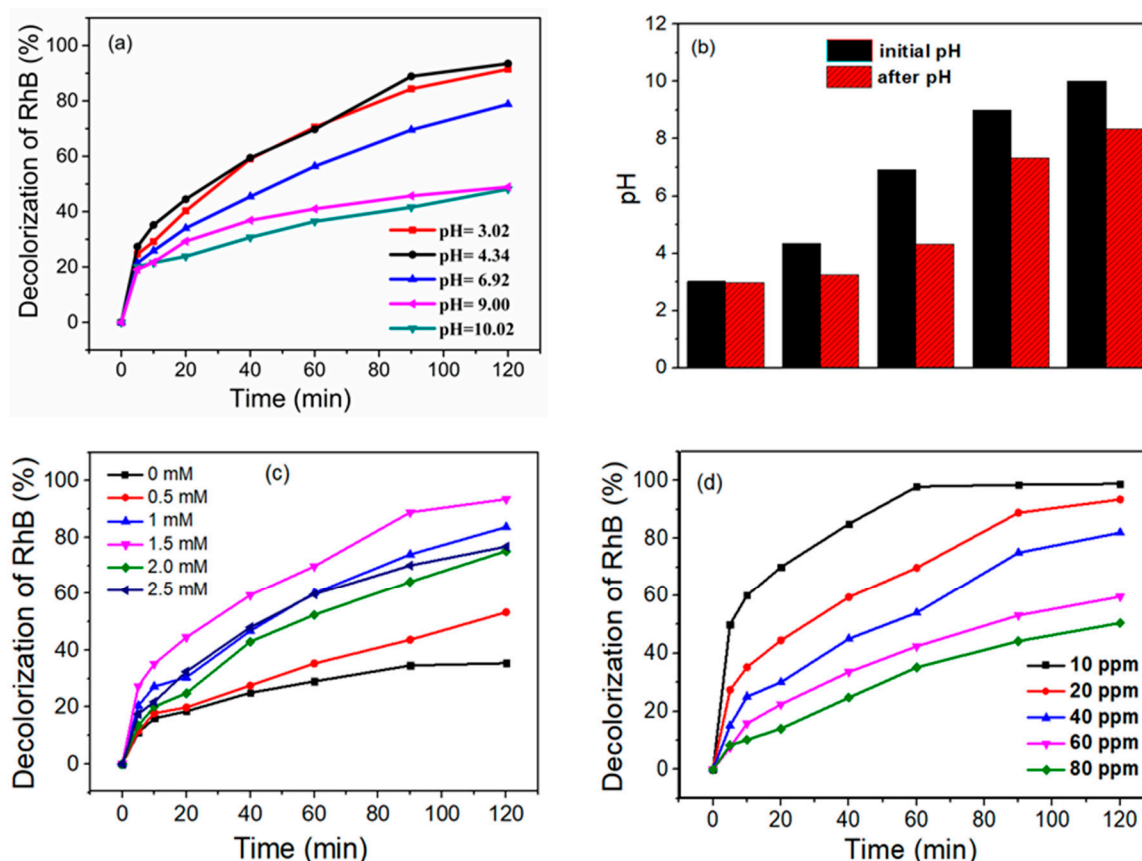


Figure 3. (a) Effect of initial pH (reaction conditions: 200 mg catalyst + 20 ppm RhB + 1.5 mM persulfate (PS)), (b) initial and after pH, (c) the influence of persulfate dosage (reaction conditions: 200 mg catalyst + 20 ppm RhB + 4.34 pH), and (d) the influence of RhB concentrations (reaction conditions: 200 mg catalyst + 1.5 mM PS + 4.34 pH).

3.3.3. Effect of RhB Concentration

The effect of various initial RhB concentration values, i.e., 10, 20, 40, 60, and 80 ppm on the degradation efficiency of RhB was examined (Figure 3d). The results highlight that the degradation efficiency of RhB slowed down with the higher-concentration solutions of RhB. At a higher RhB concentration, the surface of the catalyst was rapidly saturated and the RhB adsorption intervened in the electron transfer process, subsequently decreasing the catalytic performance. Additionally, RhB molecules and intermediates were competing for limited surface-bound radicals and reactive species on the catalyst surface under the higher concentrations of dye, thus inhibiting the overall degradation efficiency of RhB. A recent report suggested that the degradation efficiency of acid orange G (AOG) decreased with increased AOG concentration when activating peroxymonosulfate using a

Co-Mn-layered double hydroxide [33]. It was also found that the degradation performance of Acid Blue 92 was inhibited at higher dye concentrations when using the thermally activated persulfate process [34].

3.3.4. Effect of Fe Species

It has been reported that PS can be homogeneously activated by iron species ($\text{Fe}^{2+}/\text{Fe}^{3+}$) and may influence the dye degradation efficiency [35]. Therefore, the effect of Fe^{2+} and Fe^{3+} ions on the RhB degradation efficiency was investigated in the $\text{Fe}_3\text{O}_4@\text{GO} + \text{K}_2\text{S}_2\text{O}_8$ system, and the results are shown in Figure S2. As presented, $\text{Fe}_3\text{O}_4@\text{GO} + \text{K}_2\text{S}_2\text{O}_8 + \text{Fe}^{2+}$ exhibited a noticeable RhB degradation efficiency, probably due to the Fe^{2+} activation role of PS. $\text{Fe}_3\text{O}_4@\text{GO} + \text{K}_2\text{S}_2\text{O}_8 + \text{Fe}^{3+}$ nearly showed the same RhB degradation efficiency as that of $\text{Fe}_3\text{O}_4@\text{GO} + \text{K}_2\text{S}_2\text{O}_8$. However, in the presence of the $\text{Fe}_3\text{O}_4@\text{GO} + \text{K}_2\text{S}_2\text{O}_8 + \text{Fe}^{2+}$ system, a higher RhB degradation percentage than the $\text{Fe}_3\text{O}_4@\text{GO} + \text{K}_2\text{S}_2\text{O}_8 + \text{Fe}^{3+}$ system was obtained at the initial stage. This indicated that Fe^{2+} produced more sulfate radicals than Fe^{3+} and it is known that Fe^{2+} is more active as a persulfate-based heterogeneous Fenton catalyst.

3.3.5. Effect of Inorganic Anions

Some inorganic ions are used as auxiliaries in the dyeing bath and typically appear in real textile wastewater samples. For example, NaCl is an electrolyte used to improve the dye diffusion rate due to its adsorption behavior onto fibers and NaHCO_3^- is responsible for increasing the pH of the dye bath. Therefore, the effect of these ions on RhB degradation was explored. As shown in Figure S3, the presence of NaCl almost did not affect the RhB degradation efficiency. The degradation percentage of RhB was the same as the control experiment degradation efficiency. This result may be attributed to the use of a lower NaCl concentration. At a lower concentration of NaCl, less reactive Cl^- species produce Cl_2^- from the reaction of SO_4^- and $\bullet\text{OH}$ [36], which might have contributed to a higher RhB degradation efficiency. This result is supported by the previous investigation by Bendjama et al. [37]. On the contrary, the RhB degradation efficiency was significantly inhibited by the addition of NaHCO_3^- in the solution. To be specific, only 40% of the RhB could be removed in the presence of HCO_3^- , which is a much lower degradation efficiency compared with using NaCl. In the AOP system, the bicarbonate ions (HCO_3^-) were used as a radical scavenger, hence HCO_3^- were involved with RhB molecules for quenching with reactive radicals, such as SO_4^- and $\bullet\text{OH}$, and generated $\text{HCO}_3^-/\text{CO}_3^-$ radicals with a lower redox potential than SO_4^- and $\bullet\text{OH}$. Furthermore, the pH of the solution reached an alkaline condition via the addition of HCO_3^- , thus the RhB degradation efficiency was decreased in the alkaline condition in this study.

3.3.6. The Effect of the Copresence of Organic Pollutants

In general, textile wastewater contains various organic substances and ions, where dyes are one of the most significant existing pollutants. The efficient treatment of wastewater may be hindered by the presence of other co-existing dyes, which compete with the target pollutant in the adsorption process. In this study, two types of dyes, namely methylene blue as a cationic dye and Orange II as an anionic dye, were selected according to their surface charge characteristics and were used in the same solution of RhB in the $\text{Fe}_3\text{O}_4@\text{GO} + \text{K}_2\text{S}_2\text{O}_8$ system; the results are shown in Figures S4 and S5, respectively. As can be seen, both spectra show the presence of the two dyes in the RhB solution. The adsorption and degradation efficiency was higher (around 95%) for the cationic dye of MB because of the strong electrostatic interaction that occurred between the positively charged surface of the cationic dye molecules and the negatively charged GO surface. In contrast, a moderate adsorption and degradation efficiency were noticed for the anionic dye of OII because of the strong electrostatic repulsion between the anionic dye molecules and the negatively charged GO surface. Thus, the systems were suitable for treating many co-existing dyes in wastewater at the same time.

3.4. Durability of Fe₃O₄@GO

Durability is considered as one of the essential parameters of the catalyst for achieving practical feasibility. Thus, the durability of Fe₃O₄@GO was investigated by conducting six successive cycles of adsorption–catalysis reuse experiments on RhB degradation in the Fe₃O₄@GO + K₂S₂O₈ system, and the results are shown in Figure 4a. It was noticed that the adsorption percentage of RhB gradually reduced from 22.67% to 18.46%, but the percentage of RhB degradation maintained above 75% after six consecutive cycle experiments. It can be seen that the RhB degradation decreased a little over the recycling experiments in the PS activation system. The poor adsorption performance was ascribed to the limitation of active sites in the dye intermediates, while the higher degradation efficiency appeared due to the possible conversion of some Fe²⁺ to Fe³⁺ oxides species occurring on the catalyst's surface. However, these results demonstrate that the Fe₃O₄@GO catalyst could be reused in the catalytic oxidation process without a significant loss of its activity and indicate that the degradation stage was more beneficial than the adsorption process. Additionally, the leaching of metals is an essential concern in persulfate-activated metal oxide nanoscale materials. Therefore, the leaching of total iron in the Fe₃O₄@GO + K₂S₂O₈ system over six successive cycle experiments was monitored, as shown in Figure 4b. Herein, the leaching amount of total iron was below 0.05 mg/L over the six cycles, which would be very suitable for the environment due to the lack of generation of any secondary pollution, following the European Union's (EU's) discharge guidelines for iron leaching values, which allows for up to 2 mg/L [38]. This outcome indicates that the PS activation system played a significant role in iron leaching recycling tests without the addition of any iron in the solution.

To some extent, the scope of RhB mineralization is also a significant parameter for practical industrial applications. Therefore, the total organic carbon (TOC) was measured due to it being a popular indicator for evaluating the mineralization efficiency of RhB in the reaction. The removal of TOC (%) in the RhB solution as a function of time was inspected (Figure 4c). The removal percentage of TOC increased to 56% within the first 10 min and directly increased with the reaction time until reaching more than 60% by 120 min. It was noticed that the dye mineralization efficiency was slower than the dye degradation performance. This can be attributed to the significant amounts of intermediates that were still present in the solution. However, the removal efficiency of TOC could be improved by adding a higher amount of persulfate concentration or increasing the reaction time. Some researchers previously reported that more than 80% of TOC removal could be achieved by using a higher persulfate concentration [39].

Fourier-transform infrared spectra (FTIR) was utilized to identify functional groups on the catalyst surface. The FTIR spectra for Fe₃O₄@GO before (black line) and after catalysis (red line) of RhB in the Fe₃O₄@GO + K₂S₂O₈ system are presented in Figure 4d. First, the typical spectrum of GO sheets were observed in the FTIR spectra of the Fe₃O₄@GO nanocomposite with an absorbance peak at 3371–3450 cm⁻¹ (stretching –OH functional groups), which indicated that an anchorage of Fe₃O₄ particles was successfully deposited onto the GO matrix. Before catalysis, the FTIR spectrum of Fe₃O₄@GO showed two significant peaks at 568 cm⁻¹ and 493 cm⁻¹ because of Fe–O (stretching mode) in Fe₃O₄. Additionally, the peak at 1579 cm⁻¹ (C–C stretching vibrations) corresponded to the aromatic ring of GO and the C–O–H bending vibrations at 1110 cm⁻¹ and was ascribed to the phenolic group in GO sheets. The FTIR spectrum of Fe₃O₄@GO after RhB degradation showed that the band intensities became stronger and remained at an almost identical position compared to the spectrum measured before the RhB degradation. These results are further proof of the excellent durability of the Fe₃O₄@GO nanocomposite along with the above two aspects on the reusability test.

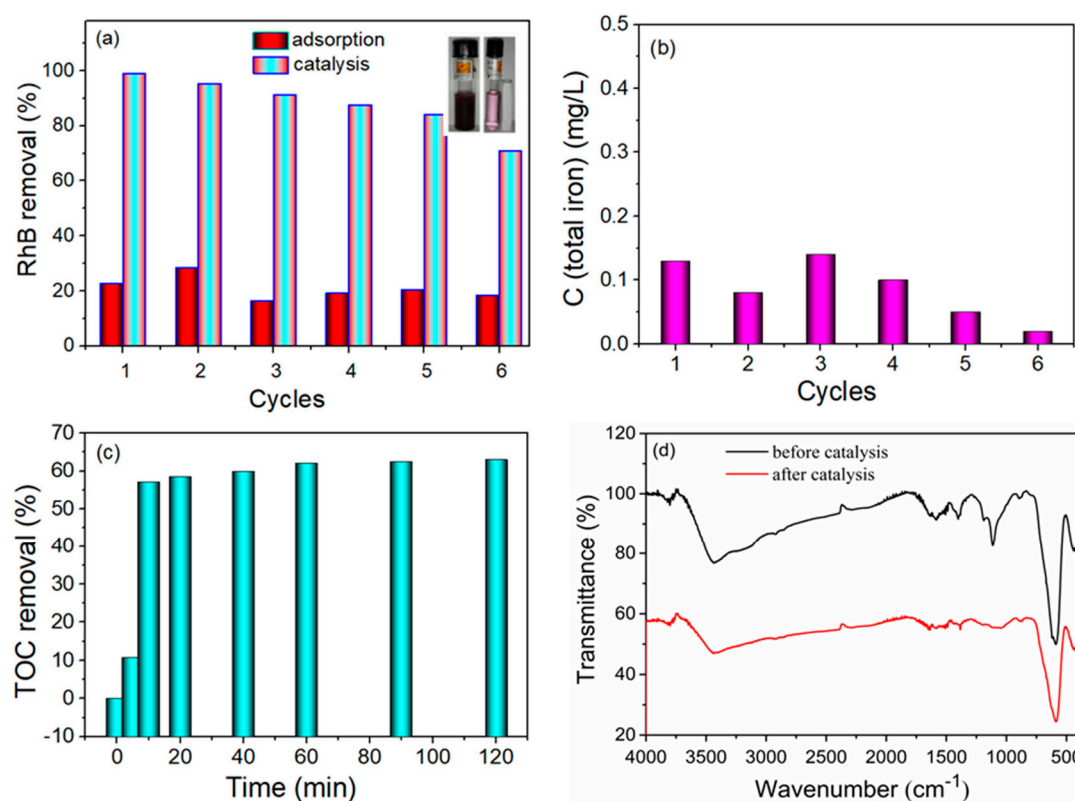


Figure 4. Adsorption–degradation cycles of (a) RhB, (b) total iron leaching, (c) total organic carbon (TOC) removal, and (d) the FTIR spectra of Fe₃O₄@GO before and after RhB degradation.

3.5. Identification of Reactive Oxygen Species (ROS)

Previous reports suggested that some reactive radical species have been produced in the PS-activation-based catalytic degradation studies. Therefore, radical quenching experiments were conducted during the RhB degradation via the addition of KI, NaN₃, MeOH, TBA, and AA to investigate the reactive oxidizing species in the Fe₃O₄@GO + K₂S₂O₈ system. It is known that TBA is used to quench only •OH radicals, whereas MeOH is used as an effective quencher for both SO₄•⁻ and •OH radicals. As shown in Figure 5a, the RhB degradation percentage was slightly decreased by the addition of TBA, which can be ascribed to the reactivity of TBA toward free radicals being higher in a liquid state rather than radicals present on the surface of a catalyst since TBA is a kind of hydrophilic substance. MeOH exhibited a slightly lower RhB degradation performance. This was attributed to the reaction rate mechanism where, for example, MeOH could react more slowly with •OH than TBA but showed a more rapid reaction rate with SO₄•⁻ than TBA. It indicates that SO₄•⁻ radicals were revealed as a primary radical species in the Fe₃O₄@GO + K₂S₂O₈ system. As can be seen, the degradation efficiency of RhB was also not affected much by the addition of AA in the solution, suggesting that the oxidation of RhB was promoted by the O₂•⁻ radical that appeared through the dissolved oxygen [40]. Fang et al. [41] reported that O₂•⁻ radicals can effectively activate the persulfate to generate SO₄•⁻ radicals, which facilitate the RhB degradation efficiency. Recently, it was observed that singlet oxygen might act as a significant ROS in the PS activation system [42]. Therefore, NaN₃ was added to the solution as the quencher for ¹O₂ radicals, which may be produced from O₂•⁻ oxidation or the transfer of energy to dissolved oxygen. The degradation efficiency of RhB was decreased slightly by the addition of NaN₃. KI has been widely used as an effective quencher for surface-bound reactive radicals, such as SO₄•⁻ and •OH. As shown in Figure 5a, the addition of KI significantly decreased the RhB degradation efficiency to 49.0%, suggesting that the oxidation of RhB was favored on the surface of Fe₃O₄@GO, which can be explained by noting the hydrophobic nature of KI was capable of capturing radicals from the catalyst surface, that resulted in a poor degradation percentage. Additionally, oxygen-containing

functional groups of GO were available on the edge of their aromatic rings, which also promoted the surface oxidation of RhB. Therefore, these results revealed that surface-bound $\text{SO}_4^{\bullet-}$ radicals were primarily responsible for almost half of the RhB degradation in this study. The present result was justified according to the previous work of Wang et al. [43].

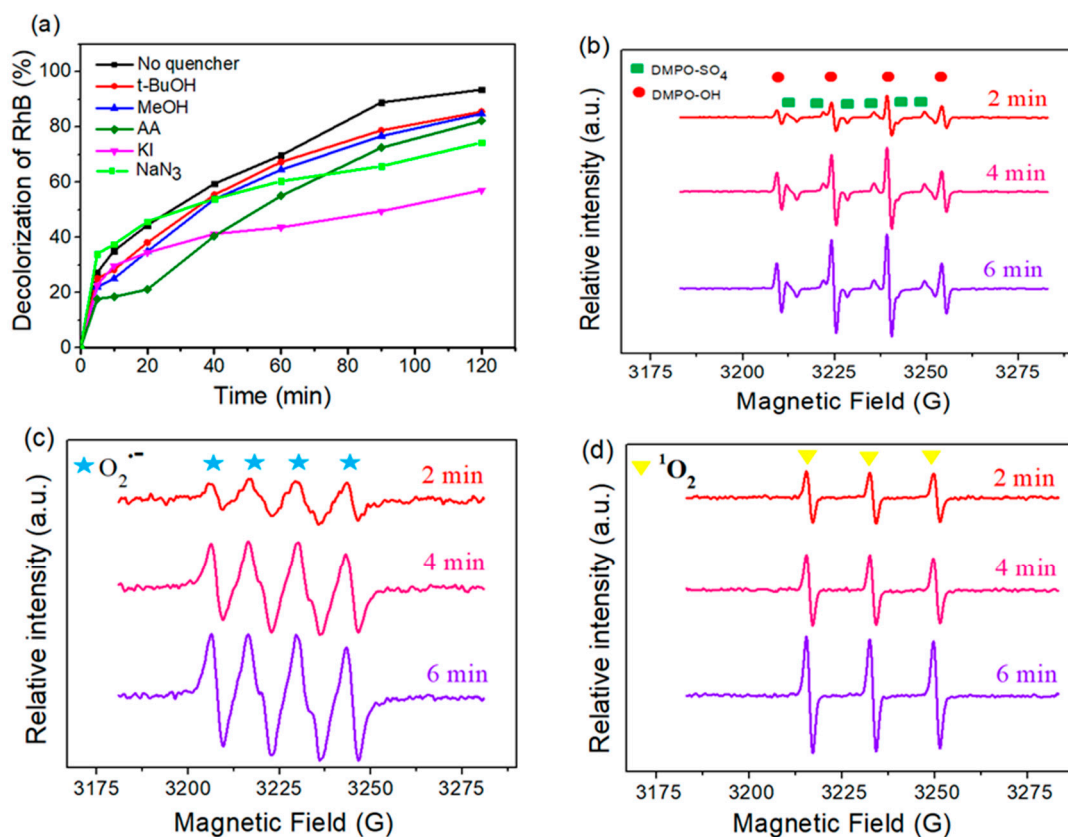


Figure 5. (a) Degradation of RhB in the presence of radical quenchers, (b) EPR spectra of DMPO- SO_4 or DMPO-OH, (c) EPR spectra of $\text{O}_2^{\bullet-}$ radicals, and (d) EPR spectra of $^1\text{O}_2$ in the $\text{Fe}_3\text{O}_4@\text{GO} + \text{K}_2\text{S}_2\text{O}_8$ system with time.

The oxidative radicals involved in the $\text{Fe}_3\text{O}_4@\text{GO} + \text{K}_2\text{S}_2\text{O}_8$ system for the RhB degradation was further verified by conducting an EPR study with spin-trapping agents, namely DMPO and TEMP. As shown in Figure 5b, the characteristic signals of DMPO- SO_4 exhibited six lines (with the ratio of intensities being 1:1:1:1:1:1 and with hyperfine splitting constants of $a\text{N} = 13.2\text{ G}$, $a\text{H} = 9.6\text{ G}$, $a\text{H} = 1.48\text{ G}$, and $a\text{H} = 0.77\text{ G}$), while the characteristic signals of DMPO-OH showed four lines (with the ratio of intensities at 1:2:2:1 and $a\text{N} = a\text{H} = 14.8\text{ G}$) [44]. The generation of $\text{O}_2^{\bullet-}$ radicals was detected using EPR signals (with a relative intensity ratio of 1:1:1:1), as shown in Figure 5c. Additionally, the identification of $^1\text{O}_2$ radicals was confirmed through the EPR signals (three lines with an intensity ratio of 1:1:1), as shown in Figure 5d. As observed, the intensities of all characteristic signals were enhanced with the increase of time from 2 to 6 min, which indicates that a large portion of the $\bullet\text{OH}$ radicals was generated from the reaction between $\text{SO}_4^{\bullet-}$ and $\text{H}_2\text{O}/\text{OH}$ [45]. The results suggested that $\text{SO}_4^{\bullet-}$, $\bullet\text{OH}$, $\text{O}_2^{\bullet-}$, and $^1\text{O}_2$ radicals were produced during the degradation of RhB degradation in the $\text{Fe}_3\text{O}_4@\text{GO} + \text{K}_2\text{S}_2\text{O}_8$ system.

3.6. Proposed Degradation Mechanism

3.6.1. RhB Degradation Pathway

The structural changes of RhB during the degradation studies over 120 min were monitored using UV-vis spectra (Figure 6a). As can be seen, the maximum absorption peak at 554 nm of RhB appeared in the visible region due to the $n \rightarrow \pi$ transition of C=N and C=C groups. Furthermore, the shoulder peaks at 258 and 354 nm in the UV region were ascribed to the benzene rings [46]. It was noticed that the maximum absorption peak intensity gradually reduced with the increase of the irradiation time, and eventually, the maximum peak disappeared within 120 min, accompanied by the blue shift and expansion of the absorption peak. This phenomenon can be ascribed to the N-de-ethylation of the RhB molecule and chromophore destruction. Additionally, the absorption peaks in the UV region first increased, and then gradually decreased due to the destruction of the benzene rings. However, no additional peak appeared during the RhB degradation studies after 120 min, implying that all the chromophore groups were destroyed. Therefore, it can be concluded that the degradation of RhB mainly occurred because of the cleavage of the chromophore structure and suggested that N-deethylation was a probable part of the RhB degradation mechanism in the $\text{Fe}_3\text{O}_4@\text{GO} + \text{K}_2\text{S}_2\text{O}_8$ system.

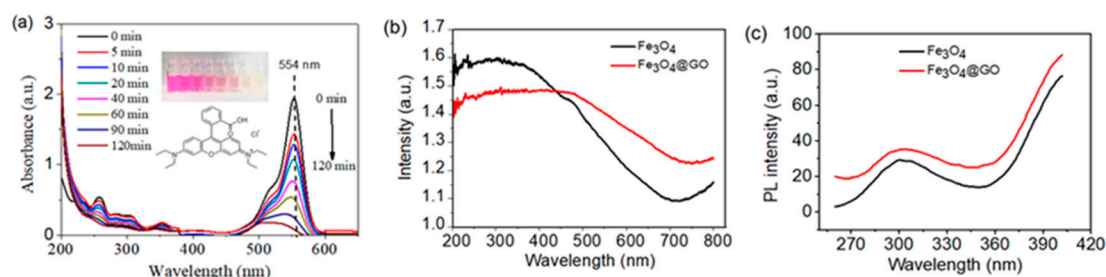


Figure 6. (a) The evolution of the UV-vis spectra during the degradation of RhB in the $\text{Fe}_3\text{O}_4@\text{GO} + \text{K}_2\text{S}_2\text{O}_8$ system (reaction conditions: 200 mg catalyst + 20 ppm RhB + 1.5 mM $\text{K}_2\text{S}_2\text{O}_8$ + 4.34 pH + agitate at room temperature (20 °C)). (b) UV-vis diffused reflectance spectra and (c) photoluminescence (PL) spectra of Fe_3O_4 and $\text{Fe}_3\text{O}_4@\text{GO}$.

To expound the enhanced PS activation ability of the $\text{Fe}_3\text{O}_4@\text{GO}$ nanocomposite, the UV-vis DRS spectra of Fe_3O_4 and GO were recorded, as shown in Figure 6b. An absorption edge at 648 nm was identified from the pristine Fe_3O_4 , which can be attributed to the value of the intrinsic bandgap (≈ 2.69 eV) in the solid solution of Fe_3O_4 [47]. Compared with Fe_3O_4 , $\text{Fe}_3\text{O}_4@\text{GO}$ exhibited a remarkable and higher intensity of visible light absorption after 450 nm. The absorption edge of $\text{Fe}_3\text{O}_4@\text{GO}$ appeared at approximately 682 nm because of the narrowing bandgap of $\text{Fe}_3\text{O}_4@\text{GO}$, which may be ascribed to the presence of a strong chemical interaction with the GO substance.

The photoluminescence (PL) spectra of $\text{Fe}_3\text{O}_4@\text{GO}$ revealed strong PL intensities over the pristine Fe_3O_4 (Figure 6c), which indicates a higher rate of recombination between the excited electrons and holes. In general, the GO sheet possessed high electrical conductivity and consequently had a higher electron mobility. Therefore, the GO sheet could easily accumulate the excited electrons from the Fe_3O_4 conduction band through a π -conjugation carbon atom, which was considered to be the most effective at achieving a higher electron-hole pair recombination rate and improved charge separation properties between the valence band and conduction band of Fe_3O_4 . These results support the higher degradation percentage of RhB that were achieved in the presence of the $\text{Fe}_3\text{O}_4@\text{GO}$ nanocomposite as an efficient catalyst for the activation of PS.

3.6.2. XPS Evidence

The elemental composition changes of Fe₃O₄@GO before and after catalytic tests were evaluated using XPS measurements, and the results are shown in Figure 7. As displayed, the full XPS spectrum survey showed the presence of different elements such as C, O, N, and Fe with the binding energies of 285 eV, 531 eV, 400 eV, and 725 eV, respectively, and their relative atomic surface concentration percentages are shown in Tables S1 and S2. In detail, the core-level spectra of O 1s was composed of three main peaks at 531 eV (Fe–O bond), 530 eV (Fe–O–C bond), and 529 eV (Fe–OH bond), indicating that the catalyst surface was enriched with different oxygen-bonded functional groups and the formation of a stable heterojunction structure between the Fe₃O₄ and the GO sheets. The XPS spectra of the Fe 2p surface exhibited two peaks with binding energies of 711 eV and 725 eV, which corresponded to the two states of Fe 2p_{3/2} and Fe 2p_{1/2}, respectively, implying the existence of Fe³⁺ in Fe₃O₄ [48]. The binding energy at 718 eV appeared in the Fe 2p surface, indicating the characteristic of a satellite peak. Overall, the successful deposition of Fe₃O₄ on GO sheets improved the surface reactivity and reduced the aggregation state of transition metal ions, which was induced by the PS-activated catalyst. The XPS spectrum of N 1s had only one deconvoluted peak with a binding energy of 400 eV, suggesting that the adsorption of N-contained RhB molecules occurred on the catalyst surface during the degradation process. This analysis supports the results of the FTIR measurements and the reuse tests on the catalyst.

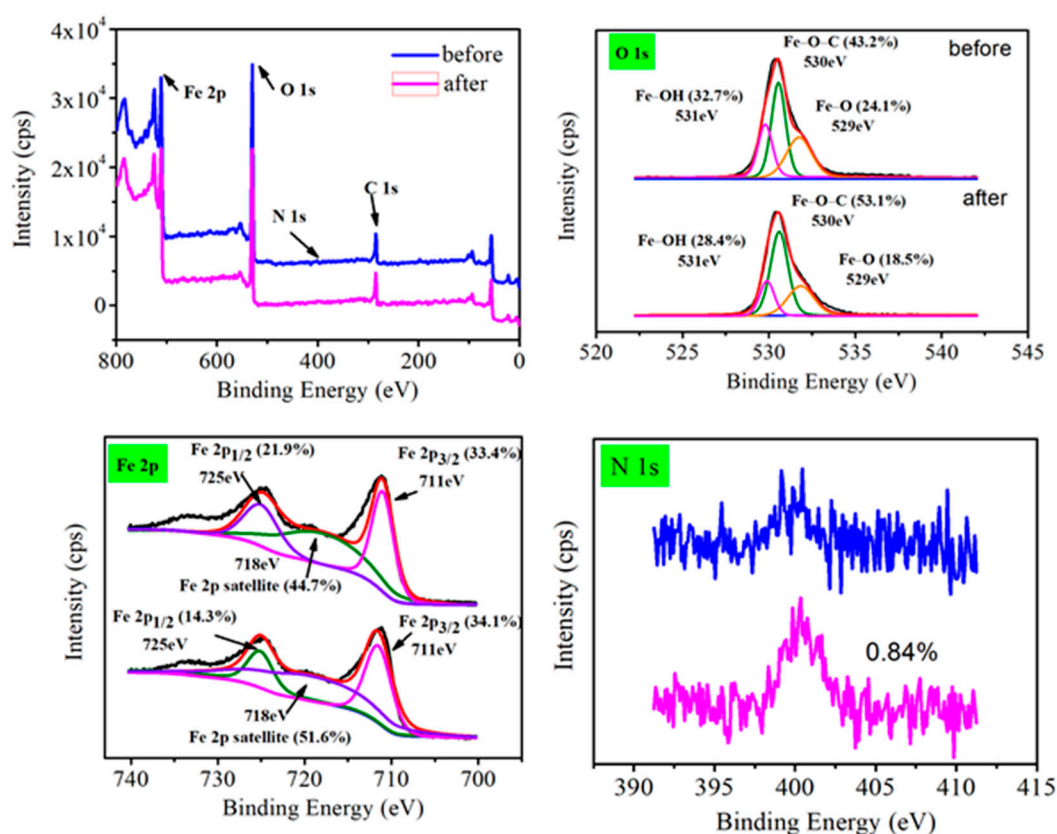


Figure 7. A full XPS spectra of Fe₃O₄@GO including O 1s, Fe 2p, and N 1s before and after the degradation of RhB.

Regarding the above discussion, a possible persulfate activation mechanism of RhB is illustrated (Figure 8). As can be seen, the reduction of the iron species and the generation of the reactive radicals were actively associated with this mechanism. The whole surface of Fe₃O₄@GO allowed PS to activate the metal sites with Fe³⁺ to produce a large amount of Fe²⁺. Then, PS was further activated by Fe²⁺ ions to yield durable surface bounded SO₄⁻ reactive radicals from the conversion between Fe²⁺ and

Fe^{3+} , as shown in Equation (3) [49]. Furthermore, $\bullet\text{OH}$ radicals could be noticed from the direct conversion of $\text{SO}_4^{\bullet-}$ through the hydrolysis reaction with H_2O (Equation (4)) [50]. These results indicate that transition metals played a crucial role in generating powerful radicals, thus accelerating the degradation efficiency.

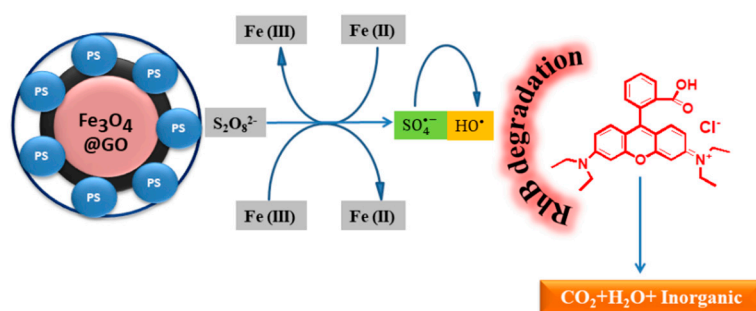


Figure 8. The possible activation mechanism of RhB in the $\text{Fe}_3\text{O}_4@\text{GO} + \text{K}_2\text{S}_2\text{O}_8$ system.

3.7. Real Wastewater Treatment Efficiency

The effectiveness of the $\text{Fe}_3\text{O}_4@\text{GO} + \text{K}_2\text{S}_2\text{O}_8$ system at treating deionized water and real wastewater treatment plant effluent is shown in Figure 9a,b. The real wastewater sample was obtained from the Minhuang wastewater treatment plant, Shanghai, China, and diluted with a selected dyes solution. The treatment procedure was conducted in optimum conditions. The final mixture was analyzed using a UV-vis spectrophotometer. Based on the results, it was demonstrated that the $\text{Fe}_3\text{O}_4@\text{GO} + \text{K}_2\text{S}_2\text{O}_8$ system showed an RhB removal percentage of up to 89% after 120 min, along with other mixture dyes, such as MB and OII, from the real wastewater sample; this indicates that this system is sufficient for practical application.

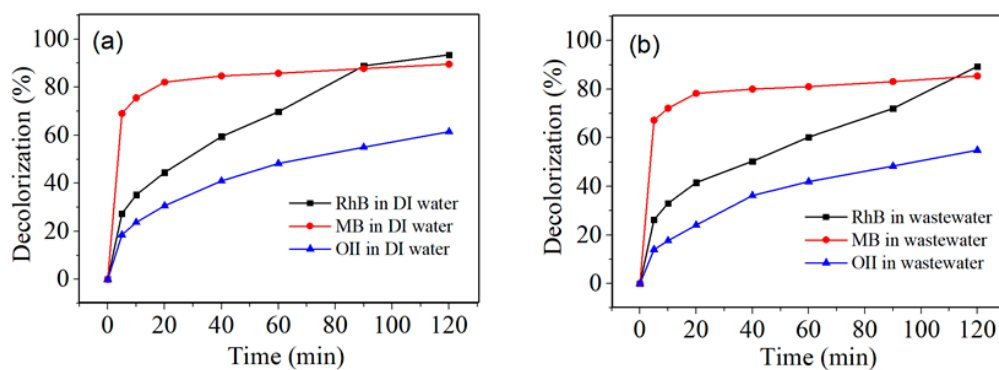


Figure 9. The catalytic efficiency of the $\text{Fe}_3\text{O}_4@\text{GO} + \text{K}_2\text{S}_2\text{O}_8$ system in (a) deionized water and (b) real wastewater effluent.

4. Conclusions

A novel Fe_3O_4 -impregnated graphene oxide ($\text{Fe}_3\text{O}_4@\text{GO}$) nanocomposite was successfully prepared using a sustainable methodology and was employed as an efficient persulfate activator for the remediation of dye pollutants in real wastewater. In this study, a nearly 100% RhB degradation efficiency was obtained in the $\text{Fe}_3\text{O}_4@\text{GO} + \text{K}_2\text{S}_2\text{O}_8$ system, and this system had an effectively degraded co-presence of organic pollutants and maintained a higher reusability property. The results indicate that the oxidation of RhB appeared on the surface of $\text{Fe}_3\text{O}_4@\text{GO}$ through the accumulation of radicals.

Nevertheless, the $\text{Fe}_3\text{O}_4@\text{GO} + \text{K}_2\text{S}_2\text{O}_8$ system showed an excellent RhB degradation efficiency under a wide range of pH values, i.e., acidic and neutral conditions. The enhanced degradation efficiency of $\text{Fe}_3\text{O}_4@\text{GO}$ was better because of the formation of a heterojunction between Fe_3O_4 and GO, which was revealed by the identification of Fe–O–C chemical bonds in the XPS spectra. This study will be a useful source for managing future challenges in treating real wastewater treatment using the persulfate-activated iron oxide–graphene composite as a potential sustainable catalyst.

Supplementary Materials: The following are available online at <http://www.mdpi.com/2073-4441/12/3/733/s1>, Figure S1: Persulfate evolution under different pH, Figure S2: Effect of iron species on RhB degradation, Figure S3: Effect of inorganics ions on RhB degradation, Figure S4: Effect of co-existing dyes MB on RhB degradation, Figure S5: Effect of co-existing dyes OII on RhB degradation, Table S1: Binding energy of detected elements for $\text{Fe}_3\text{O}_4@\text{GO}$, Table S2: Atomic surface concentration of detected elements for $\text{Fe}_3\text{O}_4@\text{GO}$.

Author Contributions: Conceptualization: Y.Z., M.N.P. and W.H.; formal analysis: Y.Z., V.N., T.Z. and M.N.P.; methodology: Y.Z. and M.N.P.; data curation: W.H. and M.N.P.; writing—original draft preparation: W.H. and M.N.P.; writing—review and editing: V.N., T.Z., and Y.Z.; supervision: Y.Z. and V.N.; funding acquisition: Y.Z. and V.N. All authors have read and agreed to the published version of the manuscript.

Funding: This study was funded by the National Natural Science Foundation of China (grant 21377039). The research activities were partially funded by the University of Salerno with the FARBS projects and by the project n. IN17GR09/INT/Italy/P-17/2016 (SP) funded by the Italian Ministry of Foreign Affairs and International Cooperation and Department of Science and Technology, Ministry of Science and Technology, Government of India. Research activities are also linked to the project n. EG16MO01 funded by the Italian Ministry of Foreign Affairs and International Cooperation with the Italian Ministry of Environment.

Acknowledgments: The Ph.D. School in Risk and Sustainability in Civil Engineering, Environmental and Construction and the Sanitary and Environmental Engineering Division (SEED) Laboratory of the University of Salerno, Italy, are acknowledged for the Ph.D. scholarship (XXXIV CYCLE) of Md. Nahid Pervez. The authors are grateful to the Sanitary Environmental Engineering Division (SEED) Laboratory of the University of Salerno Directed by Prof. Vincenzo Naddeo for providing the facilities and part of the research funds.

Conflicts of Interest: The authors declare no conflict of interest.

References

1. Contreras, M.; Grande-Tovar, C.D.; Vallejo, W.; Chaves-López, C. Bio-Removal of Methylene Blue from Aqueous Solution by *Galactomyces geotrichum* KL20A. *Water* **2019**, *11*, 282. [[CrossRef](#)]
2. Pervez, M.N.; Stylios, G.K. Investigating the synthesis and characterization of a novel “green” H_2O_2 -assisted, water-soluble chitosan/polyvinyl alcohol nanofiber for environmental end uses. *Nanomaterials* **2018**, *8*, 395. [[CrossRef](#)]
3. Park, J.H.; Shin, D.S.; Lee, J.K. Treatment of High-Strength Animal Industrial Wastewater Using Photo-Assisted Fenton Oxidation Coupled to Photocatalytic Technology. *Water* **2019**, *11*, 1553. [[CrossRef](#)]
4. Martínez-López, S.; Lucas-Abellán, C.; Serrano-Martínez, A.; Mercader-Ros, M.T.; Cuartero, N.; Navarro, P.; Pérez, S.; Gabaldón, J.A.; Gómez-López, V.M. Pulsed light for a cleaner dyeing industry: azo dye degradation by an advanced oxidation process driven by pulsed light. *J. Clean. Prod.* **2019**, *217*, 757–766. [[CrossRef](#)]
5. Hou, X.; Zhan, G.; Huang, X.; Wang, N.; Ai, Z.; Zhang, L. Persulfate activation induced by ascorbic acid for efficient organic pollutants oxidation. *Chem. Eng. J.* **2020**, *382*, 122355. [[CrossRef](#)]
6. Liu, X.; Yuan, B.; Zou, J.; Wu, L.; Dai, L.; Ma, H.; Li, K.; Ma, J. Cu (II)-enhanced degradation of acid orange 7 by Fe (II)-activated persulfate with hydroxylamine over a wide pH range. *Chemosphere* **2020**, *238*, 124533. [[CrossRef](#)]
7. Pervez, M.N.; Telegin, F.Y.; Cai, Y.; Xia, D.; Zarra, T.; Naddeo, V. Efficient Degradation of Mordant Blue 9 Using the Fenton-Activated Persulfate System. *Water* **2019**, *11*, 2532. [[CrossRef](#)]
8. Zhang, P.; Tan, X.; Liu, S.; Liu, Y.; Zeng, G.; Ye, S.; Yin, Z.; Hu, X.; Liu, N. Catalytic degradation of estrogen by persulfate activated with iron-doped graphitic biochar: Process variables effects and matrix effects. *Chem. Eng. J.* **2019**, *378*, 122141. [[CrossRef](#)]
9. Deng, J.; Feng, S.; Ma, X.; Tan, C.; Wang, H.; Zhou, S.; Zhang, T.; Li, J. Heterogeneous degradation of orange II with peroxymonosulfate activated by ordered mesoporous MnFe_2O_4 . *Sep. Purif. Technol.* **2016**, *167*, 181–189. [[CrossRef](#)]
10. Wang, Y.; Sun, H.; Ang, H.M.; Tadó, M.O.; Wang, S. Magnetic Fe_3O_4 /carbon sphere/cobalt composites for catalytic oxidation of phenol solutions with sulfate radicals. *Chem. Eng. J.* **2014**, *245*, 1–9. [[CrossRef](#)]

11. Yu, D.; Wu, M.; Hu, Q.; Wang, L.; Lv, C.; Zhang, L. Iron-based metal-organic frameworks as novel platforms for catalytic ozonation of organic pollutant: Efficiency and mechanism. *J. Hazard. Mater.* **2019**, *367*, 456–464. [[CrossRef](#)] [[PubMed](#)]
12. Liu, Z.; Li, X.; Rao, Z.; Hu, F. Treatment of landfill leachate biochemical effluent using the nano-Fe₃O₄/Na₂S₂O₈ system: Oxidation performance, wastewater spectral analysis, and activator characterization. *J. Environ. Manag.* **2018**, *208*, 159–168. [[CrossRef](#)] [[PubMed](#)]
13. Peng, G.; Zhang, M.; Deng, S.; Shan, D.; He, Q.; Yu, G. Adsorption and catalytic oxidation of pharmaceuticals by nitrogen-doped reduced graphene oxide/Fe₃O₄ nanocomposite. *Chem. Eng. J.* **2018**, *341*, 361–370. [[CrossRef](#)]
14. Kang, J.; Zhang, H.; Duan, X.; Sun, H.; Tan, X.; Wang, S. Nickel in hierarchically structured nitrogen-doped graphene for robust and promoted degradation of antibiotics. *J. Clean. Prod.* **2019**, *218*, 202–211. [[CrossRef](#)]
15. Yan, J.; Cen, J.-M.; Tan, X.-C.; Tan, S.-F.; Wu, Y.-Y.; Zhang, H.; Wang, Q. Determination of trace rhodamine B by spectrofluorometry and magnetic solid phase extraction based on a 3D reduced graphene oxide composite. *Anal. Methods* **2017**, *9*, 5433–5440. [[CrossRef](#)]
16. Yao, Y.; Cai, Y.; Lu, F.; Wei, F.; Wang, X.; Wang, S. Magnetic recoverable MnFe₂O₄ and MnFe₂O₄-graphene hybrid as heterogeneous catalysts of peroxymonosulfate activation for efficient degradation of aqueous organic pollutants. *J. Hazard. Mater.* **2014**, *270*, 61–70. [[CrossRef](#)] [[PubMed](#)]
17. Tran, H.V.; Bui, L.T.; Dinh, T.T.; Le, D.H.; Huynh, C.D.; Trinh, A.X. Graphene oxide/Fe₃O₄/chitosan nanocomposite: A recoverable and recyclable adsorbent for organic dyes removal. application to methylene blue. *Mater. Res. Express* **2017**, *4*, 035701. [[CrossRef](#)]
18. Ojha, D.P.; Joshi, M.K.; Kim, H.J. Photo-Fenton degradation of organic pollutants using a zinc oxide decorated iron oxide/reduced graphene oxide nanocomposite. *Ceram. Int.* **2017**, *43*, 1290–1297. [[CrossRef](#)]
19. Gong, X.-B. Degradation of dye wastewater by persulfate activated with Fe₃O₄/graphene nanocomposite. *J. Water Reuse Desalin.* **2016**, *6*, 553–561. [[CrossRef](#)]
20. Jain, R.; Mathur, M.; Sikarwar, S.; Mittal, A. Removal of the hazardous dye rhodamine B through photocatalytic and adsorption treatments. *J. Environ. Manag.* **2007**, *85*, 956–964. [[CrossRef](#)]
21. Hummers, W.S.; Offeman, R.E. Preparation of graphitic oxide. *J. Am. Chem. Soc.* **1958**, *80*, 1339. [[CrossRef](#)]
22. Sellers, R.M. Spectrophotometric determination of hydrogen peroxide using potassium titanium(IV) oxalate. *Analyst* **1980**, *105*, 950–954. [[CrossRef](#)]
23. Kim, D.H.; Bokare, A.D.; Koo, M.S.; Choi, W. Heterogeneous catalytic oxidation of as(iii) on nonferrous metal oxides in the presence of H₂O₂. *Environ. Sci. Technol.* **2015**, *49*, 3506–3513. [[CrossRef](#)] [[PubMed](#)]
24. Czili, H.; Horvath, A. Applicability of coumarin for detecting and measuring hydroxyl radicals generated by photoexcitation of TiO₂ nanoparticles. *Appl. Catal. B-Environ.* **2008**, *81*, 295–302. [[CrossRef](#)]
25. Rabani, J.; Mulac, W.A.; Matheson, M.S. The pulse radiolysis of aqueous tetranitromethane. I. rate constants and the extinction coefficient of eaq-. II. oxygenated solutions. *J. Phys. Chem.* **1965**, *69*, 53–70. [[CrossRef](#)]
26. Yang, X.; Chen, W.; Huang, J.; Zhou, Y.; Zhu, Y.; Li, C. Rapid degradation of methylene blue in a novel heterogeneous Fe₃O₄@rGO@TiO₂-catalyzed photo-Fenton system. *Sci. Rep.* **2015**, *5*, 10632. [[CrossRef](#)]
27. Gan, L.; Geng, A.; Xu, L.; Chen, M.; Wang, L.; Liu, J.; Han, S.; Mei, C.; Zhong, Q. The fabrication of bio-renewable and recyclable cellulose based carbon microspheres incorporated by CoFe₂O₄ and the photocatalytic properties. *J. Clean. Prod.* **2018**, *196*, 594–603. [[CrossRef](#)]
28. Romero, A.; Santos, A.; Vicente, F.; González, C. Diuron abatement using activated persulphate: Effect of pH, Fe (II) and oxidant dosage. *Chem. Eng. J.* **2010**, *162*, 257–265. [[CrossRef](#)]
29. Liang, C.; Wang, Z.-S.; Bruell, C.J. Influence of pH on persulfate oxidation of TCE at ambient temperatures. *Chemosphere* **2007**, *66*, 106–113. [[CrossRef](#)]
30. Xu, Y.; Wang, Y.; Wan, J.; Ma, Y. Reduced graphene oxide-supported metal organic framework as a synergistic catalyst for enhanced performance on persulfate induced degradation of trichlorophenol. *Chemosphere* **2020**, *240*, 124849. [[CrossRef](#)]
31. Yan, J.; Lei, M.; Zhu, L.; Anjum, M.N.; Zou, J.; Tang, H. Degradation of sulfamonomethoxine with Fe₃O₄ magnetic nanoparticles as heterogeneous activator of persulfate. *J. Hazard. Mater.* **2011**, *186*, 1398–1404. [[CrossRef](#)] [[PubMed](#)]
32. Gong, F.; Wang, L.; Li, D.; Zhou, F.; Yao, Y.; Lu, W.; Huang, S.; Chen, W. An effective heterogeneous iron-based catalyst to activate peroxymonosulfate for organic contaminants removal. *Chem. Eng. J.* **2015**, *267*, 102–110. [[CrossRef](#)]

33. Zhao, X.; Niu, C.; Zhang, L.; Guo, H.; Wen, X.; Liang, C.; Zeng, G. Co-Mn layered double hydroxide as an effective heterogeneous catalyst for degradation of organic dyes by activation of peroxymonosulfate. *Chemosphere* **2018**, *204*, 11–21. [[CrossRef](#)] [[PubMed](#)]
34. Ahmadi, S.; Igwegbe, C.A.; Rahdar, S. The application of thermally activated persulfate for degradation of acid blue 92 in aqueous solution. *Int. J. Ind. Chem.* **2019**, *10*, 1–12. [[CrossRef](#)]
35. Liang, C.; Bruell, C.J.; Marley, M.C.; Sperry, K.L. Persulfate oxidation for in situ remediation of TCE. II. activated by chelated ferrous ion. *Chemosphere*. **2004**, *55*, 1225–1233. [[CrossRef](#)] [[PubMed](#)]
36. Chen, Y.; Yan, J.; Ouyang, D.; Qian, L.; Han, L.; Chen, M. Heterogeneously catalyzed persulfate by CuMgFe layered double oxide for the degradation of phenol. *Appl. Catal. A-Gen.* **2017**, *538*, 19–26. [[CrossRef](#)]
37. Bendjama, H.; Merouani, S.; Hamdaoui, O.; Bouhelassa, M. Using photoactivated acetone for the degradation of chlorazol black in aqueous solutions: Impact of mineral and organic additives. *Sci. Total. Environ.* **2019**, *653*, 833–838. [[CrossRef](#)]
38. Dong, Z.; Zhang, Q.; Chen, B.-Y.; Hong, J. Oxidation of bisphenol A by persulfate via Fe₃O₄-α-MnO₂ nanoflower-like catalyst: Mechanism and efficiency. *Chem. Eng. J.* **2019**, *357*, 337–347. [[CrossRef](#)]
39. Yan, J.; Gao, W.; Dong, M.; Han, L.; Qian, L.; Nathanail, C.P.; Chen, M. Degradation of trichloroethylene by activated persulfate using a reduced graphene oxide supported magnetite nanoparticle. *Chem. Eng. J.* **2016**, *295*, 309–316. [[CrossRef](#)]
40. Lv, J.; Hu, Q.; Cao, C.; Zhao, Y. Modulation of valence band maximum edge and photocatalytic activity of BiOX by incorporation of halides. *Chemosphere* **2018**, *191*, 427–437. [[CrossRef](#)]
41. Fang, G.-D.; Dionysiou, D.D.; Al-Abed, S.R.; Zhou, D.-M. Superoxide radical driving the activation of persulfate by magnetite nanoparticles: Implications for the degradation of PCBs. *Appl. Catal. B-Environ.* **2013**, *129*, 325–332. [[CrossRef](#)]
42. Cheng, X.; Guo, H.; Zhang, Y.; Wu, X.; Liu, Y. Non-photochemical production of singlet oxygen via activation of persulfate by carbon nanotubes. *Water. Res.* **2017**, *113*, 80–88. [[CrossRef](#)] [[PubMed](#)]
43. Wang, X.; Qin, Y.; Zhu, L.; Tang, H. Nitrogen-doped reduced graphene oxide as a bifunctional material for removing bisphenols: Synergistic effect between adsorption and catalysis. *Environ. Sci. Technol.* **2015**, *49*, 6855–6864. [[CrossRef](#)] [[PubMed](#)]
44. Tang, L.; Liu, Y.; Wang, J.; Zeng, G.; Deng, Y.; Dong, H.; Feng, H.; Wang, J.; Peng, B. Enhanced activation process of persulfate by mesoporous carbon for degradation of aqueous organic pollutants: Electron transfer mechanism. *Appl. Catal. B Environ.* **2018**, *231*, 1–10. [[CrossRef](#)]
45. Zhu, C.; Liu, F.; Ling, C.; Jiang, H.; Wu, H.; Li, A. Growth of graphene-supported hollow cobalt sulfide nanocrystals via MOF-templated ligand exchange as surface-bound radical sinks for highly efficient bisphenol A degradation. *Appl. Catal. B-Environ.* **2019**, *242*, 238–248. [[CrossRef](#)]
46. Wang, Y.; Li, F.; Xue, T.; Liu, C.; Yuan, D.; Qi, F.; Xu, B. Heterogeneous activation of peroxymonosulfate by hierarchical CuBi₂O₄ to generate reactive oxygen species for refractory organic compounds degradation: Morphology and surface chemistry derived reaction and its mechanism. *Environ. Sci. Pollut. Res.* **2018**, *25*, 4419–4434. [[CrossRef](#)] [[PubMed](#)]
47. Radoń, A.; Drygała, A.; Hawełek, Ł.; Łukowiec, D. Structure and optical properties of Fe₃O₄ nanoparticles synthesized by co-precipitation method with different organic modifiers. *Mater. Charact.* **2017**, *131*, 148–156. [[CrossRef](#)]
48. Zhu, Y.; Yue, M.; Natarajan, V.; Kong, L.; Ma, L.; Zhang, Y.; Zhao, Q.; Zhan, J. Efficient activation of persulfate by Fe₃O₄@ β-cyclodextrin nanocomposite for removal of bisphenol A. *RSC Adv.* **2018**, *8*, 14879–14887. [[CrossRef](#)]
49. Gao, Y.; Zhang, Z.; Li, S.; Liu, J.; Yao, L.; Li, Y.; Zhang, H. Insights into the mechanism of heterogeneous activation of persulfate with a clay/iron-based catalyst under visible LED light irradiation. *Appl. Catal. B-Environ.* **2016**, *185*, 22–30. [[CrossRef](#)]
50. Jiang, J.; Zhang, D.; Zhang, H.; Yu, K.; Li, N.; Zheng, G. Degradation mechanism study of fluoroquinolones in UV/Fe²⁺/peroxydisulfate by on-line mass spectrometry. *Chemosphere* **2019**. [[CrossRef](#)]

